

RESEARCH ARTICLE

10.1002/2015JA021267

Plasma waves around separatrix in collisionless magnetic reconnection with weak guide field

Yangao Chen^{1,2}, Keizo Fujimoto³, Chijie Xiao¹, and Hantao Ji^{2,4}

Key Points:

- Beam excited electrostatic and electromagnetic waves around the separatrix
- ES waves with distinct speeds in the inflow and outflow regions
- EM waves are excited due to the beam-driven whistler instability

Correspondence to:

Y. Chen,
chenyg07@pku.edu.cn

Citation:

Chen, Y., K. Fujimoto, C. Xiao, and H. Ji (2015), Plasma waves around separatrix in collisionless magnetic reconnection with weak guide field, *J. Geophys. Res. Space Physics*, 120, 6309–6319, doi:10.1002/2015JA021267.

Received 27 MAR 2015

Accepted 25 JUN 2015

Accepted article online 29 JUN 2015

Published online 19 AUG 2015

¹State Key Laboratory of Nuclear Physics and Technology, School of Physics, and Fusion Simulation Center, Peking University, Beijing, China, ²Center for Magnetic Self-Organization, Princeton Plasma Physics Laboratory, Princeton University, Princeton, New Jersey, USA, ³Division of Theoretical Astronomy, National Astronomical Observatory of Japan, Mitaka, Japan, ⁴Laboratory for Space Environment and Physical Sciences, Harbin Institute of Technology, Harbin, China

Abstract Electrostatic and electromagnetic waves excited by electron beam around the separatrix region are analyzed in detail during the collisionless magnetic reconnection with a weak guide field by using 2-D particle-in-cell simulation with the adaptive mesh refinement. Broadband electrostatic waves are excited both in the inflow and outflow regions around the separatrices due to the electron bump-on-tail, two-stream, and Buneman instabilities. In contrast, the quasi-monochromatic electromagnetic waves are excited only in the inflow side of the separatrices due to a beam-driven whistler instability. The localization of the whistler waves is attributed to the nonuniformity of the out-of-plane magnetic field B_y . The whistler instability is suppressed in the outflow side where B_y is too small for the oblique propagation. The electrostatic waves with distinct speeds can explain the in situ spacecraft observations. From the causality point of view, the waves are generated as the consequence of the electron bulk acceleration to thermalize the particles through wave-particle interactions. These simulation results provide guidance to analyze high-resolution wave observations during reconnection in the ongoing and upcoming satellite missions, as well as in dedicated laboratory experiments.

1. Introduction

Magnetic reconnection is a basic physical process in the numerous space, solar, astrophysical, and laboratory plasmas, accompanied by the magnetic energy converting to the plasma thermal energy and kinetic energy [Yamada *et al.*, 2010; Fujimoto *et al.*, 2011]. Wave-particle interactions can contribute to transformation from magnetic energy to kinetic and thermal energy. Plasma waves near the magnetic reconnection region were reported in recent satellite observations such as electrostatic solitary waves [Cattell *et al.*, 2005; Viberg *et al.*, 2013] and lower hybrid wave [Zhou *et al.*, 2011] in the magnetotail reconnection site and whistler waves in the magnetopause [Deng and Matsumoto, 2001; Tang *et al.*, 2013] and in the magnetotail [Wei *et al.*, 2007]. Both electrostatic [Carter *et al.*, 2001] and electromagnetic waves [Ji *et al.*, 2004] were also diagnosed in the laboratory reconnection experiments. The knowledge of the waves is helpful for understanding the reconnection dynamics.

Plasma waves associated with magnetic reconnection are frequently observed around the separatrix region, where streaming electrons were detected by in situ observations [Asano *et al.*, 2008; Zhou *et al.*, 2011; Graham *et al.*, 2015] and by numerical simulations [Cattell *et al.*, 2005; Pritchett, 2005; Lapenta *et al.*, 2011; Fujimoto, 2014]. Beam-plasma interactions have been investigated thoroughly from the theoretical point of view [Chen, 1987; Stix, 1992; Sauer and Sydora, 2010; Jara-Almonte *et al.*, 2014] and are well recognized to give rise to many electrostatic and electromagnetic instabilities, such as Buneman instability, electron two-stream instability, and whistler instability. More recently, a nonlinear mechanism was used to explain the whistler emission [Goldman *et al.*, 2014]. Most of the previous particle-in-cell (PIC) simulations of collisionless reconnection have employed relatively larger background (lobe) density than the realistic value in the Earth magnetotail [Kivelson and Russell, 1995], because of the limitation of computer resources. The larger background density corresponds to higher value of the upstream plasma beta, which results in lower Alfvén velocity compared to the thermal velocity in the outflow exhaust, as shown by Fujimoto [Fujimoto, 2014]. Therefore, it is expected that in most of the previous PIC simulations the diversity of the beam instabilities has been suppressed unrealistically in the reconnection region. In fact, it has been difficult in usual PIC simulations to reproduce the wave

observations from satellites, where a variety of waves were detected simultaneously in the separatrix region [Viberg *et al.*, 2013; Graham *et al.*, 2015].

The PIC simulation with the adaptive mesh refinement (AMR) enables us to use much larger size of the computational cells in the upstream region than that in the center of the current sheet [Fujimoto, 2011]. This indicates that the realistic low-beta plasma can be easily realized in the lobe region with sufficient number of particles per cell by using the AMR-PIC model. Recent large-scale AMR-PIC simulations have revealed that an electrostatic potential jump is generated in the separatrix region due to the ion-electron decoupling motions [Fujimoto, 2014]. The potential jump accelerates the electrons strongly in the inflow direction and forms an electrical double layer. The accelerated electrons can interact with the background electrons, ions, and the outflow electrons so that a variety of wave activities are expected.

Fujimoto [Fujimoto, 2014] investigated only the inflow side of the separatrix region of the antiparallel reconnection. However, intense wave activities are also observed in simulation in the outflow side of the separatrix region. Furthermore, weak guide field exists in some cases in magnetotail reconnection [Oieroset *et al.*, 2001; Xiao *et al.*, 2007] and in most cases in magnetopause reconnection [Deng and Matsumoto, 2001; Tang *et al.*, 2013].

In this work, we focus on the electrostatic and electromagnetic waves in detail around the separatrices in collisionless magnetic reconnection with a weak guide field. The simulation model will be introduced in section 2. In section 3, details of both the electrostatic and electromagnetic wave generation, propagation, and distribution around the separatrix region are analyzed, which helps us to understand the acceleration and thermalization of the particles, and thus the energy transformation of magnetic reconnection process. Finally, the conclusion of the current study is given in section 4.

2. Simulation Model

The simulations are performed using a 2-D electromagnetic PIC model with the AMR and particle splitting-coalescence technique [Fujimoto, 2011]. An open boundary condition is employed for both the upstream and downstream directions so that both the particles and magnetic flux can cross the system boundary in association with the evolution of magnetic reconnection [Fujimoto, 2014]. We consider a Harris-type current sheet with the magnetic field $\vec{B}(z) = -B_0 \tanh(z/\delta) \hat{e}_x + B_g \hat{e}_y$ and density profile $n(z) = n_0 \text{sech}^2(z/\delta) + n_b \tanh^2(z/\delta)$, where we choose $B_g = 0.3B_0$, $\delta = 0.5\lambda_i$, and $n_b = 0.044n_0$. Hereafter, unless otherwise noted, the magnetic field strength, plasma density, length scale, plasma velocity, timescale, and temperature are normalized by B_0 , n_0 , $\lambda_i (= c/\omega_{pi})$, $v_{Ai} (= B_0/\sqrt{\mu_0 n_0 m_i})$, ω_{ci}^{-1} , and $\frac{1}{2} m_i v_{Ai}^2$, respectively. The ion-to-electron mass ratio and velocity of light are $m_i/m_e = 400$ and $c/V_A = 68$, respectively; thus, $\omega_{pe}/\omega_{ce} = 3.4$. The temperature ratios are $T_{0i}/T_{0e} = 5.0$, $T_{bi}/T_{be} = 1.0$, and $T_{be}/T_{0e} = 1.0$, where T_{0s} and T_{bs} are the current sheet and background temperatures, respectively, for the species s .

The domain size is $L_x \times L_z = 131\lambda_i \times 65.5\lambda_i$ which is entirely covered by the base-level cells with $\Delta_{LB} = 0.032\lambda_i$ and can be subdivided locally into finer cells up to the dynamic range level with $\Delta_{LD} = 0.008\lambda_i$. A computational cell is subdivided when the Debye length λ_{De} and out-of-plane electron velocity V_{ey} calculated at the center of the cell satisfy the condition of $\Delta_L \geq 2.0\lambda_{De}$ or $V_y \geq 2.0V_A$. The time interval is fixed to $\Delta t = 8.0 \times 10^{-5} \omega_{ci}^{-1}$ through all the levels, and it satisfied the Courant condition at the dynamic range level. The number of particles per cell is controlled to be 150 approximately. These relatively realistic parameters of m_i/m_e and n_b/n_0 make the $\beta \simeq 3.5 \times 10^{-3}$ in the simulation in the lobe region comparable to that from observations $\beta \simeq 3 \times 10^{-3}$ [Kivelson and Russell, 1995], which lead to more intense acceleration of the electrons in the reconnection region which facilitates the beam-driven instabilities.

3. Results

Magnetic reconnection is initiated with a small perturbation to the magnetic field, which produces the X line at the center of the system [Fujimoto, 2006]. We focus on the wave structure around the separatrices at $t\omega_{ci} = 29$ when magnetic reconnection becomes quasi-steady as shown in Figure 1. Considering the wave can only propagate in the XZ plane (in plane) in the 2-D simulation, we decompose both the electric and magnetic field into in-plane and out-of-plane (y component) parts. Thus, the wave propagation angle defined as the angle between the in-plane wave vector and the total magnetic field line can be calculated from $\tan \theta = \frac{B_y}{\sqrt{B_x^2 + B_z^2}}$. The

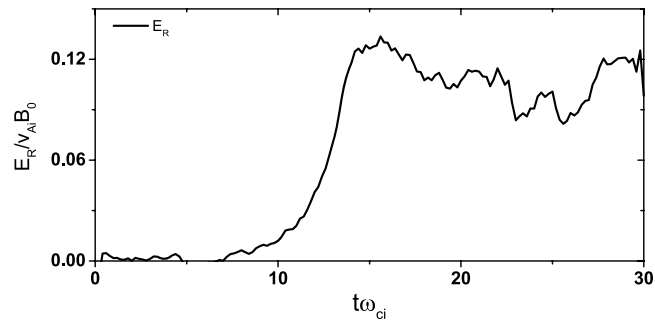


Figure 1. The time evolution of the reconnection rate E_R , which is normalized by $v_{Ai}B_0$ at the upstream inflow region.

in-plane parallel electric field $E_{\parallel} \left(\equiv \frac{E_x B_x + E_z B_z}{\sqrt{B_x^2 + B_z^2}} \right)$ and out-of-plane electric field E_y in ion frame ($E_{y,rest} + (\vec{v}_i \times \vec{B})_y$, where \vec{v}_i is the ion bulk velocity in the Cartesian coordinate) are shown in Figures 2a and 2b, where the color contour represents the electric fields and the blue arrow denotes the magnetic field lines. The wave activities are remarkable both for E_{\parallel} and E_y , around the separatrices. These waves propagate almost along the ambient field line, namely, the wave vector \vec{k} is almost along E_{\parallel} and perpendicular to E_y , which indicates that the E_{\parallel} waves are mainly electrostatic, while the E_y waves are electromagnetic. The asymmetry of the wave activity in the guide field magnetic reconnection with the wave activity region is much wider in the second and fourth quadrants than that in the first and third ones since the electron outflow is dominant in the second and fourth quadrant due to the $j_{ex} \times B_g$ force [Pritchett and Coroniti, 2004; Cattell et al., 2005; Eastwood et al., 2010]. Figure 2c shows the parallel (solid line) and perpendicular (dash line) bulk velocity of the ions (blue line) and the electrons (green line) along a field line indicated by L_1 in Figures 2a and 2b. It is clearly seen that the electrons tend to move along the field line, while the ions pass mainly across the field line. This implies that the electrons are strongly magnetized to the ambient magnetic field, while the ions are not completely magnetized in this region. In fact, the ion gyroradius is comparable with the typical width of the separatrix region. The decoupling motions between the ions and the electrons result in a local potential jump in the separatrix region, leading to the formation of a double layer [Fujimoto, 2014].

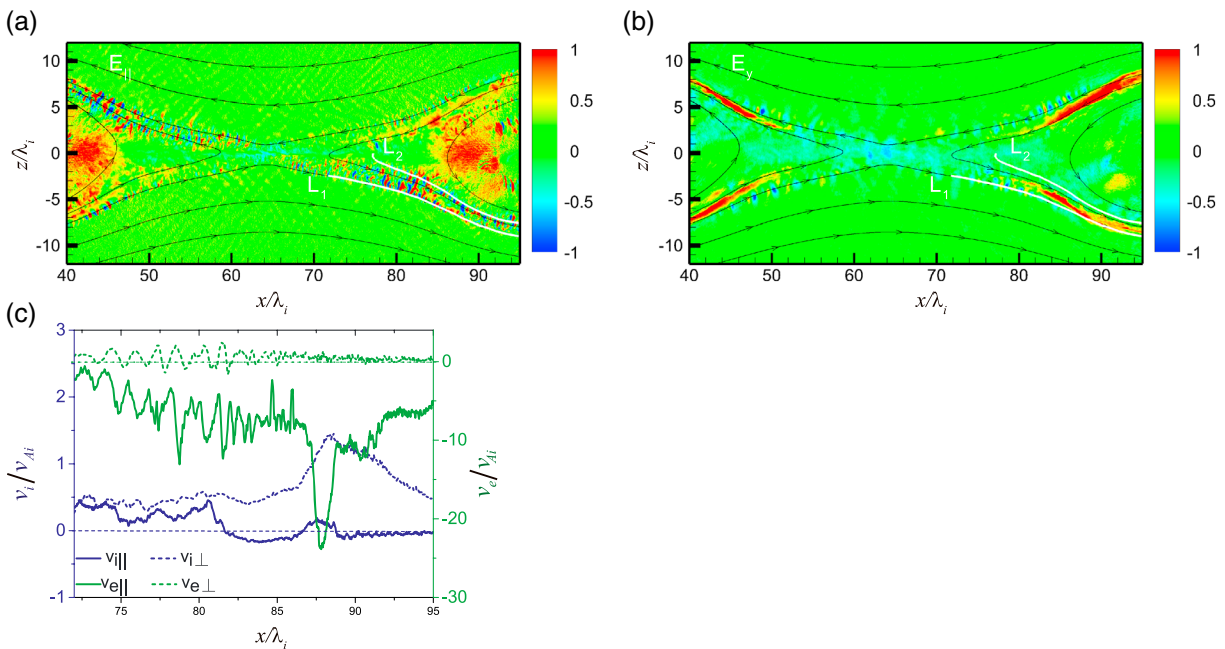


Figure 2. Two-dimensional contour plots at $t\omega_{ci} = 29$ around the X line of (a) the in-plane parallel electric field E_{\parallel} and (b) the out-of-plane electric field E_y in the ion frame. (c) Line profiles along a field line denoted by L_1 of the bulk velocity for the ions (blue curve) and the electrons (green curve) in the parallel (solid curve) and perpendicular (dashed curve) directions.

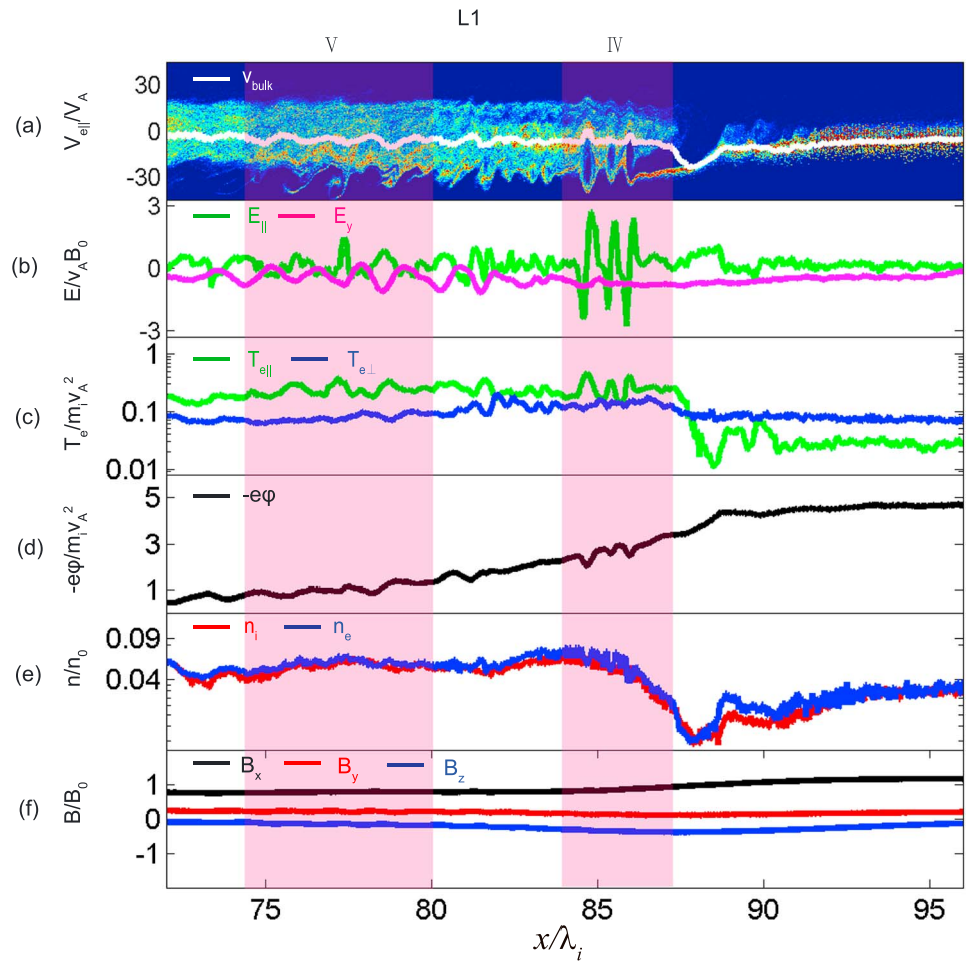


Figure 3. Phase space distribution and line profiles along the field line indicated by L1 in Figures 2a and 2b at $t\omega_{ci} = 29$. (a) Electron phase space distribution with bulk flow (solid line), thermal velocity (dash line); (b) E_{\parallel} (green line) and E_y (magenta line); (c) electron temperature in parallel (green) and perpendicular (blue) direction; (d) electrostatic potential; (e) ion (red) and electron (blue) density; and (f) magnetic field in x (black), y (red), and z (blue) directions.

Figure 3 shows the electron phase space distribution and line profiles along the field line indicated by the white curve (L1) in Figures 2a and 2b. In Figures 3a, the thickness of the curves to sample the electrons is $0.04\lambda_{i1}$, which is small enough to resolve the electron dynamics. Along the L_1 , the electrons are moving toward the X line in bulk (Figure 3a) so that this is the inflow side of the separatrix region. The wave activities are significant at $x < 86$ for both the E_{\parallel} and E_y (Figure 3b) and thermalize the electrons both in the parallel and perpendicular directions (Figure 3c). The wave generation is considered due to an intense electron beam produced by the local potential jump formed at $86 < x < 88$ (Figure 3d), which leads to a density cavity (Figure 3e) observed frequently in the reconnection region [Cattell et al., 2005; Zhou et al., 2011; Tang et al., 2013]. Regardless of guide field reconnection, the B_y component is relatively small $B_y \approx 0.2$ in this region, where the reconnection Hall field is imposed in the opposite direction to the guide field. Therefore, the propagation angle of the waves is $\theta \approx 14^\circ$ with respect to the ambient magnetic field. These properties along the field line (L_1) are basically consistent with those for the antiparallel reconnection case [Fujimoto, 2014].

The main difference in the guide field reconnection from the antiparallel case is the asymmetric wave activities around the separatrices [Pritchett and Coroniti, 2004; Cattell et al., 2005; Eastwood et al., 2010]. In particular, the asymmetric property is very remarkable in the current simulation where the realistic plasma beta is employed in the upstream (lobe) region. As shown in Figure 2a, the E_{\parallel} waves have large amplitudes even deep inside the exhaust in the second and fourth quadrants. Figure 4 shows the profiles along a field line L2 which passes through the inside of the exhaust and the region where the E_{\parallel} waves are active. One can see clearly in Figure 4a that the electrons are moving away from the center of the current sheet in bulk. This is a different property

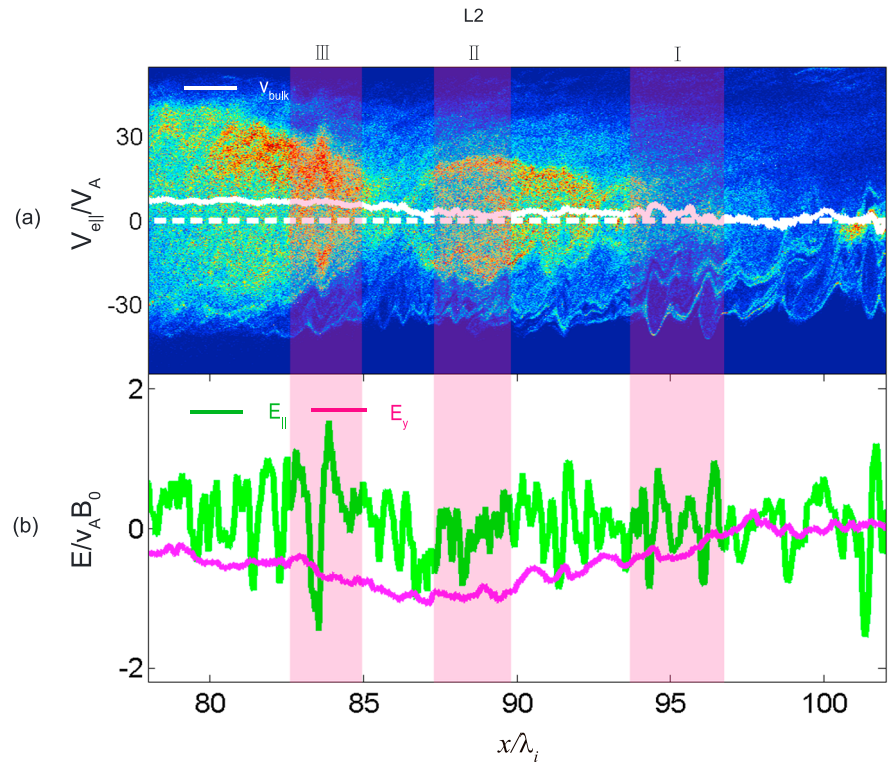


Figure 4. Phase space distribution and E field profile along the field line indicated by L2 in Figures 1a and 1b at $t\omega_{ci} = 29$. (a) Electron phase space distribution with bulk flow (solid line); the dash line is the location where $v_{e||} = 0$, (b) $E_{||}$ (green line) and E_y (magenta line).

from the electrons along L1 where they are traveling toward the X line. To be specific, from the electron phase space distribution (Figure 4a), one can find that the electron bulk flow ($v_{be||}$, the solid line) near the central current sheet at $x < 85$ is $v_{be||} \approx 7$ accompanied by a peak at $v_{e||} \approx 25$, which means there is a thermalized electron beam moving outward at this region. Meanwhile, a clear phase space hole (between $v_{e||} \approx -11$ and $v_{e||} \approx 21$) is formed at $83 < x < 84$ with central velocity at $v_{e||} \approx 5$, which is much smaller than that in the inflow region along L1. At the same time, the $E_{||}$ wave shows a remarkable bipolar structure, which corresponds to the phase space hole at this region as shown in Figure 4b. These evidences indicate that this wave is propagating much slower than that in the inflow region. This point can be figured out by considering the electrostatic wave to be a phase hole in the phase space; thus, the wave phase speed can be inferred by the phase hole velocity, which will also be clearly clarified from the dispersion relationship in the later section. As the electrons keep moving outward to the region ($87 < x < 90$), where the electron potential is relatively constant and the averaged electron bulk ($\bar{v}_{be||}$) flow is small, $\bar{v}_{be||} \approx 2.5$ in this case, the electrons that move toward the current sheet center become remarkable. The interaction between these two electron beams ($v_{b1} \approx 16, v_{b2} \approx -12$) is accompanied by a relatively weak $E_{||}$ wave structure. More far away from the current sheet center after this encounter region at $x > 94$, the electron beam generated by the electron potential jump at $106 < x < 108$ (not shown here) moving toward the current sheet center is dominant (the averaged electron bulk flow $\bar{v}_{be||} < 0$). Clear phase space hole accompanied by an obvious $E_{||}$ wave is formed at this region with central velocity at $v_{e||} \approx 30$, which is similar to that along L1. Based on the electron phase space distribution along L2, at least three kinds of $E_{||}$ wave with distinct speeds are simultaneously identified around the separatrix region related to the asymmetric electron outflow beam, electron inflow beam, and their interaction.

In order to investigate the relationship between the waves and the electron beams, we have performed linear wave analyses based on fully kinetic dispersion relation, as shown in the Appendix A. During the linear analyses, the ions are treated as unmagnetized particles forming isotropic Maxwellian distribution, while the electrons are assumed as magnetized particles consisting of a background part (subscript 0) and a

beam part (subscript 1), as shown in equation (1). Each component of the electron distribution function has anisotropic temperature.

$$f_i = n_i \left(\frac{m_i}{2\pi T_i} \right)^{\frac{3}{2}} e^{-\frac{m_i v_i^2}{2T_i}}$$

$$f_e = \sum_{k=0,1} n_{e,k} \left(\frac{m_e}{2\pi T_{ek,\parallel}} \right)^{\frac{1}{2}} \left(\frac{m_e}{2\pi T_{ek,\perp}} \right) e^{-\frac{m_e}{2} \left(\frac{(v_{be,k} - v_{e\parallel,k})^2}{T_{e\parallel,k}} + \frac{v_{e\perp,k}^2}{T_{e\perp,k}} \right)} \quad (1)$$

Here $n_i (= n_{e,0} + n_{e,1})$, v_i , and T_i are the ion density, particle velocity, and temperature, respectively. $v_{be,k}$, $v_{e\parallel,k}$, $v_{e\perp,k}$, $T_{e\parallel,k}$, and $T_{e\perp,k}$ are the electron bulk velocity, parallel and perpendicular components of electron particle velocity, and temperature for the species k . The parameters will be specified later for each wave. Since the E_{\parallel} wave is almost electrostatic, thus only the parallel component in the dielectric tensor D_{xx} (formula A1) is used (x is along k direction). The linear dispersion relation is solved for $\omega = \omega_r + i\gamma$ by using the Newton iteration.

Five typical regions of wave activity are analyzed in detail as marked by I to V in Figures 3 and 4. The time history of each E_{\parallel} wave structure and the spectrum are shown in Figure 5. In the outflow region along L2 (Figures 5a–5f), three E_{\parallel} waves with distinct speeds are diagnosed. The first wave spectrum has a peak at $\omega \simeq 0.8\omega_{pe}^*$, and $k_{\parallel}\lambda_e^* \simeq 1.6$ at $94 < x/\lambda_i < 97$ (region I), where ω_{pe}^* and λ_e^* are the local electron plasma frequency and inertial length so that this wave is recognized as the Langmuir wave. The linear analysis results show that the wave spectrum in the simulation is consistent with the dispersion of the electron bump-on-tail instability (beam velocity less than the thermal velocity of the background plasma). The parameters used for the analysis are taken at $x/\lambda_i \simeq 95$ in region I such as $n_i = 0.04$, $T_i = 0.6$, $n_{e1} = 0.003$, $v_{be1} = -39$, $T_{e\parallel,1} = 0.07$, $T_{e\perp,1} = 0.26$, $v_{be0} = 0$, $T_{e\parallel,0} = 0.74$, and $T_{e\perp,0} = 1$. The averaged $f_e(v_{e\parallel})$ at this region is shown by the red line in Figure 5i. The second E_{\parallel} wave has $\omega \simeq 0.1\omega_{pe}^*$, and $k_{\parallel}\lambda_e^* \simeq 1.5$ at $86 < x/\lambda_i < 90$ (region II). We selected the dispersion of the electron two-stream instability considering the encounter of the inflow and outflow electron beams at this region. The parameters used for the analysis are obtained at $x/\lambda_i \simeq 88$ in region II with $n_i = 0.077$, $T_i = 0.8$, $n_{e1} = 0.032$, $v_{be1} = 16$, $T_{e\parallel,1} = 0.21$, $T_{e\perp,1} = 0.47$, $v_{be0} = -12$, $T_{e\parallel,0} = 0.23$, and $T_{e\perp,0} = 1.3$. The averaged $f_e(v_{e\parallel})$ at this region is shown by the green line in Figure 5i. The wave spectrum and the linear analysis show good consistency. An even slower E_{\parallel} wave with $\omega \simeq 0.02\omega_{pe}^*$ and $k_{\parallel}\lambda_e^* \simeq 1.0$ was generated at $80 < x < 85$ (region III). Ion effects are needed to take into account because of very low frequency ($\omega \simeq 0.4\omega_{pi}^*$) at this region, where ω_{pi}^* is the local ion plasma frequency. Thus, the dispersion of Buneman instability was used for the linear analysis with the parameters taken from $x/\lambda_i \simeq 84$ in region III with $n_i = 0.084$, $T_i = 1.3$, $n_{e1} = 0.05$, $v_{be1} = 21$, $T_{e\parallel,1} = 0.3$, $T_{e\perp,1} = 0.94$, $v_{be0} = -11$, $T_{e\parallel,0} = 0.5$, and $T_{e\perp,0} = 0.92$. The averaged electron distribution function $f_e(v_{e\parallel})$ at this region is shown by the blue line in Figure 5i. The frequency spectrum shown in Figure 5f is the result after filtering the DC and high k components since the data resolution is a little bit low in this frequency range. This well-matched wave spectrum and dispersion relation confirmed that the E_{\parallel} wave in region III is generated by the Buneman instability.

Similar analysis was accomplished for the E_{\parallel} wave in the inflow region along L1 (Figures 5g and 5h), the dominated E_{\parallel} wave is $\omega \simeq 0.6\omega_{pe}^*$, and $k_{\parallel}\lambda_e^* \simeq 1.8$ at $83 < x/\lambda_i < 86$ (region IV). However, the background electron temperature in this region is much smaller than that in region I, as shown in Figure 5j. In other words, in region IV, the beam velocity is larger than the thermal velocity of the background plasma; thus, the dispersion of the electron two-stream instability rather than the bump-on-tail instability was used to access the simulation results. The parameters are $n_i = 0.024$, $T_i = 0.07$, $n_{e1} = 0.004$, $v_{be1} = -30$, $T_{e\parallel,1} = 0.05$, $T_{e\perp,1} = 0.2$, $v_{be0} = 0$, $T_{e\parallel,0} = 0.2$, and $T_{e\perp,0} = 0.4$. The wave spectrum and the linear analysis match well. Moreover, this wave keeps moving to region V ($75 < x/\lambda_i < 80$) and superpose but not coalescence with another E_{\parallel} wave (not shown here) with $\omega \simeq 0.3\omega_{pe}^*$ and $k_{\parallel}\lambda_e^* \simeq 2.0$. The waves in region V also matches the dispersion of the electron two-stream instability by using the local plasma and beam parameters $n_i = 0.056$, $T_i = 0.76$, $n_{e1} = 0.015$, $v_{be1} = -18$, $T_{e\parallel,1} = 0.05$, $T_{e\perp,1} = 0.2$, $v_{be0} = 0$, $T_{e\parallel,0} = 0.15$, and $T_{e\perp,0} = 0.2$. This lower velocity electron beam originates from the slowing down of the higher-velocity electron beam.

Electron beams not only excite the E_{\parallel} wave but also can generate E_y wave, as shown in Figure 2b and region V in Figure 3a. The time history of the E_y wave structure and polarization are shown in Figures 6a and 6b. A clear wave structure moving toward the X line is shown in Figure 6a, and this direction is the same as the direction of the electron beam. Figure 6b shows that the E_y wave is clearly right hand polarized. Considering this right-hand polarized nature of the electromagnetic wave and the wave frequency range between the ion

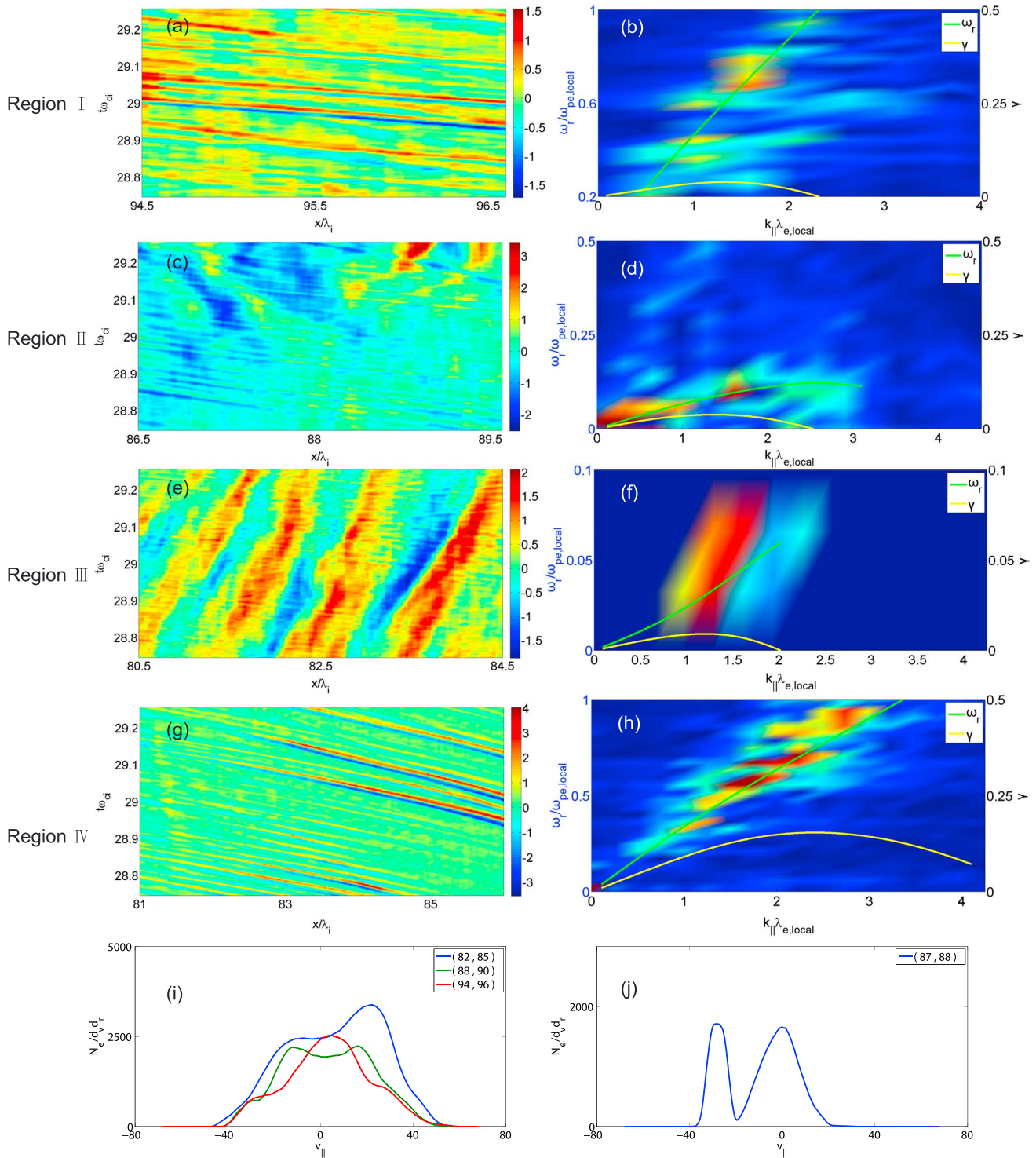


Figure 5. (a–j) Time history and frequency spectrum of $E_{||}$ in regions I, II, III, and IV. In the frequency spectrum frames shown in Figures 5b, 5d, 5f, and 5h, the green and yellow lines are real and imaginary parts of the dispersion relationship from the linear analysis. Figures 5b, 5d, and 5f are bump-on-tail, two-stream, Buneman instabilities, respectively. The electron beam density, parallel velocity, and parallel temperature used here are from the averaged distribution function in the outflow region, as shown in Figure 5i. Electron two-stream instability (Figure 5h) by using the averaged distribution function in the inflow region, as shown in Figure 5j.

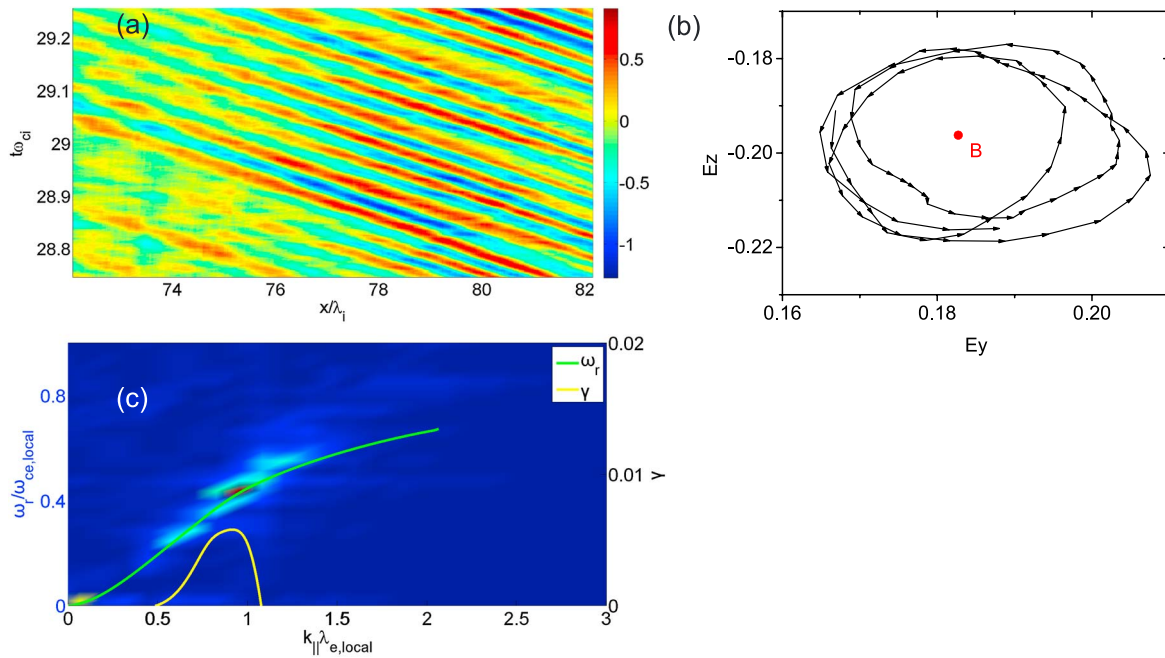


Figure 6. Electromagnetic wave properties in the inflow region(L1). (a) The time history of E_y (ion frame). (b) The hodograph of the electric field. (c) The wave spectrum of E_y superposed by the theoretical dispersion curve of the beam-driven whistler instability.

cyclotron and electron cyclotron frequencies, we expect this wave is the whistler wave. In order to analyze this electromagnetic ($\vec{k} \cdot \vec{E} = 0$) wave spectrum, we have used the full form of the kinetic linear dispersion, as shown in equation (A1), where \mathbf{D} is the dielectric tensor with elements specified by (A1)–(A5). The parameters in equation (1) are taken from region V with $n_i = 0.052$, $T_i = 0.85$, $n_{e1} = 0.004$, $v_{be1} = -35$, $T_{e||,1} = 0.059$, $T_{e\perp,1} = 0.1$, $v_{be0} = -2$, $T_{e||,0} = 0.19$, $T_{e\perp,0} = 0.2$, $B_x = 0.74$, $B_y = 0.2$, and $B_z = -0.12$, as shown in Figure 5i. The well-matched dispersion relation and the wave spectrum (Figure 6c) confirm the beam excited whistler wave.

Finally, we consider the factors that leads to the localized E_y waves, as shown in Figure 2b. It turns out that the local electron beam parameters, such as velocity, density, temperature, and local magnetic field, determine whether the wave can grow or not, as shown in Figure 7. The larger electron beam velocity slightly enhances the real frequency and dramatically influences the growth rate (Figure 7a). The smaller wave propagation angle $\left(\tan \theta = \frac{B_y}{\sqrt{B_x^2 + B_z^2}} \right)$ corresponds to the smaller (even zero) growth rate and slowly growing up of real frequency (Figure 7b). The higher-electron beam density gives rise to a larger real frequency and quickly changed growth rate (Figure 7c). Finally, the parallel temperature of the beam has little influence on the real frequency but affects the growth rate a lot, as shown in Figure 7d. The red dots are the parameters used in the linear analysis, such as $v_b = 0.53c$, $\cos \theta = 0.97$. From wave spectrum (Figure 6c), we can find $\omega = 0.43\omega_{pe}^*$, $k\lambda_e^* = 0.96$, thus $\omega \approx kv_b \cos \theta$. This mechanism is also called Cerenkov instability in the previous study [Sauer and Sydora, 2010]. For the outflow separatrix region, the B_y is very week so that this is the main reason why the whistler wave is localized in the inflow region.

The electron beams in the magnetic reconnection process generate the broadband electrostatic waves with frequency range $(0.02 - 1) \omega_{pe,local}$ and quasi-monochromatic electromagnetic wave with frequency near $0.4 \omega_{ce,local}$ around the separatrix region, which explains the wave properties of the in situ observations. For example, when $|B_0| = 30$ nT, and $n_0 = 10 \text{ cm}^{-3}$ by following the parameters from observation [Graham et al., 2015], then we can get the wave phase velocity 270 km/s to 5400 km/s based on Figures 5b, 5d, 5f, and 5h, which basically match the observation results from 120 km/ to 1500 km/s. In the inflow side separatrix, both electrostatic and electromagnetic waves are excited by the electron beam, where the beam is generated by the potential jump. However, in the outflow side of the separatrix region, only the electrostatic waves are generated because of critical conditions, especially B_y distribution, for the whistler wave.

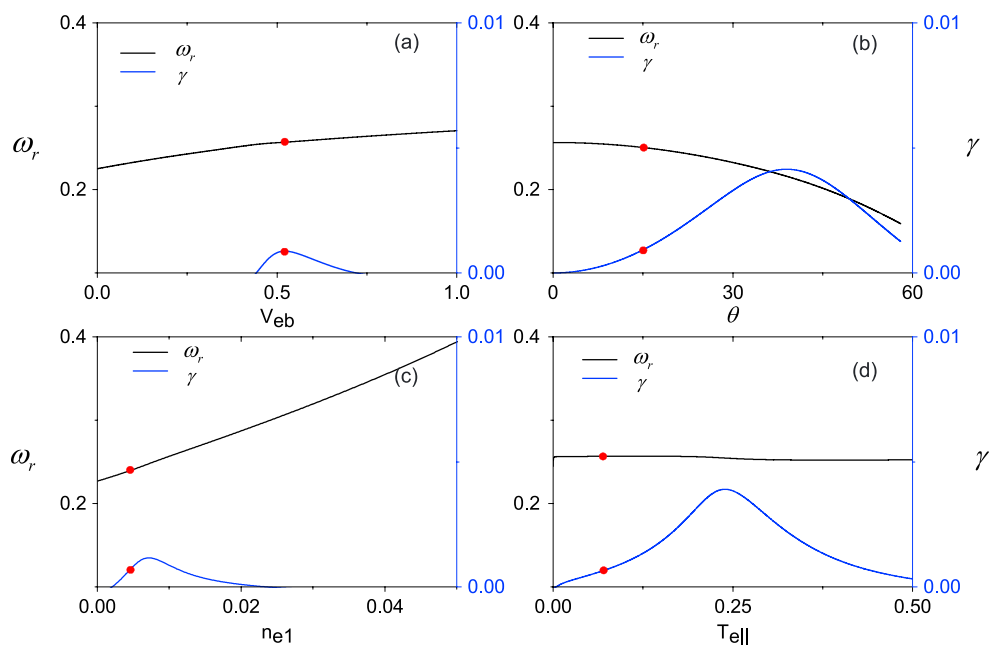


Figure 7. Parameter dependencies of the beam-driven whistler instability. (a–d) The beam velocity, wave propagation angle with respect to the magnetic field, beam density, and parallel beam temperature, respectively. The red dots are the parameters used in the linear analysis.

4. Summary and Discussion

The present study has revealed that the electrostatic waves with distinct phase speeds are excited by the electron bump-on-tail, electron two-stream, and Buneman instabilities. The bump-on-tail and two-stream instabilities give rise to the fast electrostatic waves. However, the Buneman instability excites slow electrostatic waves. The beam velocity determines the phase velocity and direction of the plasma electrostatic waves. The present results explain the widely observed electrostatic solitary wave (ESW) accompanied by distinct phase speeds moving toward or outward the X line. On the other hand, beam-excited whistler wave is localized in the inflow side of the separatrices. The theoretical linear analyses indicate that this localized excitation is attributed mainly to the nonuniformity of the out-of-plane magnetic field.

The plasma waves are the consequence of the bulk acceleration of the electrons, which are superposed by the inflow electron beam accelerated by electrostatic potential jump around the separatrix region and the outflow electron beam accelerated by the reconnection electrical field near X line. These beam-plasma instabilities can help to understand the simultaneously observation of ESWs and electron beams both in the magnetotail [Zhou *et al.*, 2011] and magnetopause [Graham *et al.*, 2015] though the higher plasma beta may suppress the growth rate of the instabilities. The $E_{||}$ wave with different phase velocities corresponding to frequency from ion plasma frequency up to electron plasma frequency will trap the particles with different velocities. This wave-particle interaction helps to convert the electron bulk flow energy into electron thermal energy. In other words, electrons get heated when they go through these wave activity regions around the separatrices. It is worthy to note that the present 2-D simulation can linearly predict the propagation angle of the whistler wave in the truly 3-D scenario by using the full dispersion relation. Based on Figure 7b, the maximum growth rate of the whistler instability is around 40° and the wave propagation direction and distribution will be more diversity in the truly 3-D situation, while the real frequency do not change significantly. This expectation can be used to guide satellite observations [Zhou *et al.*, 2011; Viberg *et al.*, 2013] as well as measurements in the laboratory experiments [Ji *et al.*, 2004; Roytershteyn *et al.*, 2013]. This work helps to understand the electron dynamics in the magnetic reconnection region. Particle thermalization and acceleration will be discussed in future work.

Appendix A: Kinetic Dispersion Relation

The Maxwell equations are linearized by using the plane wave approximation. One can get

$$\left[\bar{\epsilon} - \left(\frac{kc}{\omega} \right)^2 \left(\bar{I} - \frac{\vec{k}\vec{k}}{k^2} \right) \right] \cdot \delta \vec{E} = 0, \quad (\text{A1})$$

where $\bar{\epsilon}$ is the dielectric tensor. k , ω , \vec{E} , and \bar{I} are the wave number, frequency, and amplitude of the wave electrical field vector and unit tensor, respectively. c is the light velocity.

$$\mathbf{D} \equiv \bar{\epsilon} - \left(\frac{kc}{\omega} \right)^2 \left(\bar{I} - \frac{\vec{k}\vec{k}}{k^2} \right) = \begin{pmatrix} D_{xx} & D_{xy} & D_{xz} \\ D_{yx} & D_{yy} & D_{yz} \\ D_{zx} & D_{zy} & D_{zz} \end{pmatrix}$$

$$\|\mathbf{D}\| = D_{xx} + \frac{2D_{xy}D_{xz}D_{yz} - D_{xz}^2D_{yy} + D_{xy}^2D_{zz}}{D_{yy}D_{zz} + D_{yz}^2} = 0 \quad (\text{A2})$$

Further, by setting the wave propagating direction as the x direction, we can get

$$D_{xx} = 1 + \frac{2\omega_{pi}^2}{k^2v_i^2} \left[1 + \xi_i Z(\xi_i) \right] + \sum_b \left[\frac{2\omega_{pe,b}^2}{k^2v_{e||,b}^2} \left[1 + \frac{T_{e||,b}}{T_{e\perp,b}} \times \sum_n \left(\xi_{e0,b} - \left(1 - \frac{T_{e\perp,b}}{T_{e||,b}} \right) \xi_{en,b} \right) I_n(\zeta) \exp(-\zeta) Z(\xi_{en,b}) \right] \right] \quad (\text{A3})$$

$$D_{yy} = 1 - \left(\frac{kc}{\omega} \right)^2 + \frac{\omega_{pi}^2}{\omega^2} \xi_i Z(\xi_i) + \sum_b \left[- \left(1 - \frac{T_{e\perp,b}}{e_{||,b}} \right) \frac{\omega_{pe,b}^2}{\omega^2} + \frac{2\omega_{pe,b}^2}{\omega^2} \right. \\ \left. \times \sum_n \left(\xi_{e0,b} - \left(1 - \frac{T_{e\perp,b}}{T_{e||,b}} \xi_{en,b} \right) \right) \left(\frac{n^2}{2\zeta} I_n + \zeta (I_n - I'_n) \right) e^{-\zeta} Z(\xi_{en,b}) \right] \quad (\text{A4})$$

$$D_{zz} = 1 - \left(\frac{kc}{\omega} \right)^2 + \frac{\omega_{pi}^2}{\omega^2} \xi_i Z(\xi_i) + \sum_b \left[- \left(1 - \frac{T_{e\perp,b}}{T_{e||,b}} \right) \frac{k^2 \omega_{pe,b}^2}{k_{||}^2 \omega^2} + \frac{2k_{\perp}^2 \omega_{pe,b}^2}{k_{||}^2 k^2 v_{e||,b}^2} \right. \\ \left. \times \left[1 + \frac{T_{e||,b}}{T_{e\perp,b}} \sum_n \left(1 - \frac{k^2 n \omega_{ce}}{k_{\perp}^2 \omega} \right)^2 \left(\xi_{e0,b} - \left(1 - \frac{T_{e\perp,b}}{T_{e||,b}} \right) \xi_{en,b} \right) \xi_{en,b} I_n e^{-\zeta} Z(\xi_{en,b}) \right] \right]$$

$$D_{xy} = -D_{yx} = \sum_b \left[-i \frac{k_{\perp}}{k} \frac{\omega_{pe,b}^2}{\omega \omega_{ce}} \sum_n \left(\xi_{e0,b} - \left(1 - \frac{T_{e\perp,b}}{T_{e||,b}} \xi_{en,b} \right) \right) (I'_n - I_n) e^{-\zeta} Z(\xi_{en,b}) \right] \quad (\text{A5})$$

$$D_{xz} = D_{zx} = \sum_b \left[2 \frac{k_{\perp}}{k_{||}} \frac{\omega_{pe,b}^2}{k^2 v_{e||,b}^2} \left[1 + \frac{T_{e||,b}}{T_{e\perp,b}} \sum_n \left(1 - \frac{k^2 n \omega_{ce}}{k_{\perp}^2 \omega} \right) \left(\xi_{e0,b} - \left(1 - \frac{T_{e\perp,b}}{T_{e||,b}} \right) \xi_{en,b} \right) \times I_n(\zeta) e^{-\zeta} Z(\xi_{en,b}) \right] \right] \quad (\text{A6})$$

$$D_{yz} = -D_{zy} = \sum_b \left[i \frac{k_{\perp}}{k k_{||}} \frac{\omega_{pe,b}^2}{\omega \omega_{ce}} \left[\sum_n \left(1 - \frac{k^2 n \omega_{ce}}{k_{\perp}^2 \omega} \right) \left(\xi_{e0,b} - \left(1 - \frac{T_{e\perp,b}}{T_{e||,b}} \right) \xi_{en,b} \right) \times (I'_n - I_n) e^{-\zeta} Z(\xi_{en,b}) \right] \right] \quad (\text{A7})$$

where $\xi_i = \frac{\omega}{k v_i}$, $\xi_{en,b} = \frac{\omega' - n \omega_{ce}}{k_{||} v_{e||,b}}$, $\omega' = \omega - k_{||} v_{e||,b}$, $\zeta = \frac{k_{\perp}^2 v_{e\perp,b}^2}{2 \omega_{ce}^2}$, and \sum_b is the summation of each electron beam component. $\omega_{pe,b}$ is the beam-plasma frequency, v_i , $v_{e||,b}$, $T_{e||,b} \left(= \frac{m_e}{2} \frac{\int (v_{e||} - v_{e||})^2 f dv}{\int f dv} \right)$, and $T_{e\perp,b} \left(= \frac{m_e}{2} \frac{\int (v_{e\perp} - v_{e\perp})^2 f dv}{\int f dv} \right)$ are the ion thermal velocity, electron beam bulk velocity, electron parallel, and perpendicular temperature, respectively. I is the Bessel function, and Z is the plasma dispersion function.

Acknowledgments

We thank the NAOJ Visiting Research Fellow Program which gave us a chance to start the current research. The simulations were carried out by Fujitsu CX400 at ITC, Nagoya University, with support from a joint research program at STEL, Nagoya University. This work was also supported by the China Scholarship Council, 201406010040, NSFC (grants 41421003 and 41274168), and 973 project (grant 2011CB811404). The results in this paper are generated from our computer simulation code as described in section 2. The data can be obtained by contacting the authors through e-mail (chenyg07@pku.edu.cn).

Yuming Wang thanks two anonymous reviewers for their assistance in evaluating this paper.

References

- Asano, Y., et al. (2008), Electron flat-top distributions around the magnetic reconnection region, *J. Geophys. Res.*, *113*, A01207, doi:10.1029/2007JA012461.
- Cattell, C., et al. (2005), Cluster observations of electron holes in association with magnetotail reconnection and comparison to simulations, *J. Geophys. Res.*, *110*, A01211, doi:10.1029/2004JA010519.
- Carter, T. A., H. Ji, F. Trintchouk, M. Yamada, and R. M. Kulsrud (2001), Measurement of lower-hybrid drift turbulence in a reconnecting current sheet, *Phys. Rev. Lett.*, *88*, 15001, doi:10.1103/PhysRevLett.88.015001.
- Chen, L. (1987), *Waves and Instabilities in Plasmas*, vol. 12, World Scientific Lecture Notes in Physics, Singapore.
- Deng, X. H., and H. Matsumoto (2001), Rapid magnetic reconnection in the Earth's magnetosphere mediated by whistler waves, *Nature*, *410*, 557–560.
- Eastwood, J. P., M. A. Shay, T. D. Phan, and M. Øieroset (2010), Asymmetry of the ion diffusion region hall electric and magnetic fields during guide field reconnection: Observations and comparison with simulations, *Phys. Rev. Lett.*, *104*, 205001, doi:10.1103/PhysRevLett.104.205001.
- Fujimoto, K. (2006), Time evolution of the electron diffusion region and the reconnection rate in fully kinetic and large system, *Phys. Plasmas*, *13*, 072904, doi:10.1063/1.2220534.
- Fujimoto, K. (2011), A new electromagnetic particle-in-cell model with adaptive mesh refinement for high-performance parallel computation, *J. Comput. Phys.*, *230*, 8508–8526.
- Fujimoto, K. (2014), Wave activities in separatrix regions of magnetic reconnection, *Geophys. Res. Lett.*, *41*, 2721–2728, doi:10.1002/2014GL059893.
- Fujimoto, M., I. Shinohara, and H. Kojima (2011), Reconnection and waves: A review with a perspective, *Space Sci. Rev.*, *160*, 123–143.
- Graham, D. B., Y. V. Khotyaintsev, A. Vaivads, and M. André (2015), Electrostatic solitary waves with distinct speeds associated with asymmetric reconnection, *Geophys. Res. Lett.*, *42*, 215–224, doi:10.1002/2014GL062538.
- Kivelson, M. G., and C. T. Russell (1995), *Introduction to Space Physics*, 588 pp., Cambridge Univ. Press, Cambridge, U. K.
- Goldman, M. V., D. L. Newman, L. Andersson, J. T. Gosling, S. Eriksson, R. Ergun, G. Lapenta, S. Markidis, and J. P. Eastwood (2014), Čerenkov emission of quasiparallel whistlers by fast electron phase-space holes during magnetic reconnection, *Phys. Rev. Lett.*, *112*, 145002.
- Jara-Almonte, J., W. Daughton, and H. Ji (2014), Debye scale turbulence within the electron diffusion layer during magnetic reconnection, *Phys. Plasmas*, *21*, 032114.
- Ji, H., S. Terry, M. Yamada, R. Kulsrud, A. Kuritsyn, and Y. Ren (2004), Electromagnetic fluctuations during fast reconnection in a laboratory plasma, *Phys. Rev. Lett.*, *92*, 115001.
- Lapenta, G., S. Markidis, A. Divin, M. V. Goldman, and D. L. Newman (2011), Bipolar electric field signatures of reconnection separatrices for a hydrogen plasma at realistic guide fields, *Geophys. Res. Lett.*, *38*, L17104, doi:10.1029/2011GL048572.
- Øieroset, M., et al. (2001), In situ detection of collisionless reconnection in the Earth's magnetotail, *Nature*, *412*, 414–417.
- Pritchett, P. L., and F. V. Coroniti (2004), Three-dimensional collisionless magnetic reconnection in the presence of a guide field, *J. Geophys. Res.*, *109*, A01220, doi:10.1029/2003JA009999.
- Pritchett, P. L. (2005), Onset and saturation of guide-field magnetic reconnection, *Phys. Plasmas*, *12*, 062301.
- Roytershteyn, V., S. Dorfman, W. Daughton, H. Ji, M. Yamada, and H. Karimabadi (2013), Electromagnetic instability of thin reconnection layers: Comparison of three-dimensional simulations with MRX observations, *Phys. Plasmas*, *20*, 061212.
- Sauer, K., and R. D. Sydora (2010), Beam-excited whistler waves at oblique propagation with relation to STEREO radiation belt observations, *Ann. Geophys.*, *28*, 1317–1325.
- Stix, T. H. (1992), *Waves in Plasmas*, Springer, New York.
- Tang, X., C. Cattell, J. Dombek, L. Dai, L. B. Wilson III, A. Breneman, and A. Hupach (2013), THEMIS observations of the magnetopause electron diffusion region: Large amplitude waves and heated electrons, *Geophys. Res. Lett.*, *40*, 2884–2890, doi:10.1002/grl.50565.
- Viberg, H., Yu. V. Khotyaintsev, A. Vaivads, M. André, and J. S. Pickett (2013), Mapping HF waves in the reconnection diffusion region, *Geophys. Res. Lett.*, *40*, 1032–1037, doi:10.1002/grl.50227.
- Wei, X. H., J. B. Cao, G. C. Zhou, O. Santolík, H. Rème, I. Dandouras, N. Cornilleau-Wehrin, E. Lucek, C. M. Carr, and A. Fazakerley (2007), Cluster observations of waves in the whistler frequency range associated with magnetic reconnection in the Earth's magnetotail, *J. Geophys. Res.*, *112*, A10225, doi:10.1029/2006JA011771.
- Xiao, C. J., et al. (2007), Satellite observations of separator-line geometry of three-dimensional magnetic reconnection, *Nat. Phys.*, *3*, 609–613.
- Yamada, M., R. Kulsrud, and H. Ji (2010), Magnetic reconnection, *Rev. Mod. Phys.*, *82*, 603–664.
- Zhou, M., Y. Pang, X. H. Deng, Z. G. Yuan, and S. Y. Huang (2011), Density cavity in magnetic reconnection diffusion region in the presence of guide field, *J. Geophys. Res.*, *116*, A06222, doi:10.1029/2010JA016324.